the dye-doped polyimide substrate before filling with the liquid-crystal medium. A liquid-crystal 'grating' made in this way is illustrated in Fig. 4. The liquid-crystal alignment induced by laser irradiation is stable and can be erased or re-written by altering the direction of the incident electric-field polarization of the laser beam.

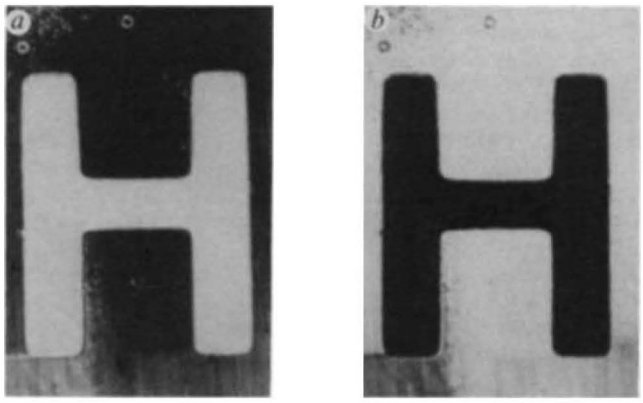

FIG. 3 A laser-aligned letter H in the liquid-crystal cell as viewed with a polarization microscope for *a*, parallel polarizers, and *b*, crossed polarizers. A mask in the shape of the letter H was placed in front of the liquid-crystal-filled cell, which was then illuminated with a 514.5-nm polarized laser at 9 W cm^{-2} for 1 min. The liquid-crystal alignment inside the letter H was along the initial alignment direction induced by rubbing the surfaces with a cloth. The liquid crystals within the illuminated background assumed a twisted nematic structure which caused a 90° rotation of the incident light polarization. The image has a height and width of 1.5 mm and 1.2 mm, respectively.

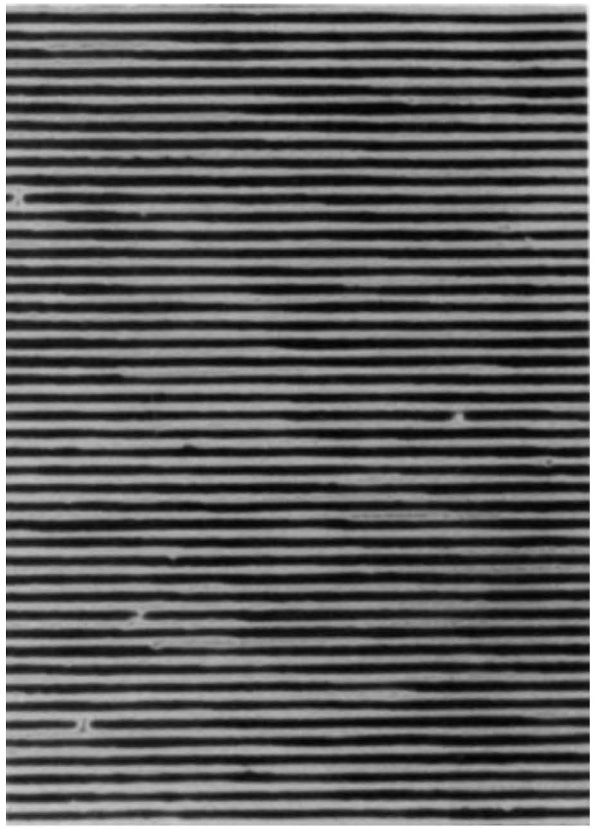

FIG. 4 A laser-aligned 10-μm grating in the liquid-crystal cell, as viewed with a polarization microscope with crossed polarizers. The cell was illuminated with a two-beam, plane-wave interference pattern with the angle between the plane waves chosen to give a fringe periodicity of 10 μm. The average incident intensity of the interfering beams onto the cell was 4 W cm^{-2}. The cell was exposed for 10 min. In this case, the cell was illuminated before filling with the liquid crystal.

An interesting aspect of our finding is that liquid crystals with a positive dielectric anisotropy are aligned perpendicular to the electric field of the laser beam. The 'memory' effect (alignment after irradiation of the dye-doped substrate) indicates that the laser-induced alignment is surface-mediated: the effect of irradiation of the dye-doped surface is apparently being 'read out' by the liquid crystal. Light-induced dye orientation and birefringence phenomena in a polymer matrix have been reported previously[4,5]. It is plausible that the orientation of liquid crystals directly reflects the state of dye orientation at the liquid-crystal/polymer interface. The mechanism of coupling between liquid-crystal molecule and dye-doped polymer is unclear at present. Our preliminary results have shown that the kinetics of laser-induced orientation is a function of dye structure, dye concentration, liquid-crystal type, incident energy density and polymer chemistry.

The possibility of controlling the orientation of liquid crystals at a spatial resolution of the order of micrometres or less suggests a number of potentially useful applications. Liquid crystals are birefringent, and switchable by either electric or magnetic fields. Diffractive optical elements can thus be made, such as phase gratings and binary holograms. Coupled with proper electrode design, optical devices useful for adaptive optics can be envisaged. Our experiments also demonstrated the use of the liquid crystal as a read-out device for the surface state. The ordering of the surface by the laser beam may have uses in molecular micro-assembly. □

Received 8 February; accepted 7 March 1991.

1. Cognard, J. *Molec. Cryst. Liq. Cryst.* **51,** 1-77 (1982).
2. De Gennes, P. G. *The Physics of Liquid Crystals* (Clarendon, Oxford, 1974).
3. Geary, J. M., Goodby, J. W., Kmetz, A. R. & Patel, J. S. *J. appl. Phys.* **62,** 4100-4108 (1987).
4. Todorov, T., Nikolova, L. & Tomova, N. *Appl. Opt.* **23,** 4309-4312 (1984).
5. Ebralidze, T. D. & Mumladze, A. N. *Appl. Opt.* **29,** 446-447 (1990).

ACKNOWLEDGEMENTS. We thank S. T. Schnelle for technical support.

Insignificant isotropic component in the moment tensor of deep earthquakes

Hitoshi Kawakatsu

Geological Survey of Japan, 1-1-3 Higashi, Tsukuba, Ibaraki 305 Japan

THE mechanism responsible for deep-focus earthquakes, which occur at depths of 300–700 km in subducting slabs, has been a long-standing problem in geophysics. Unlike shallow earthquakes, deep earthquakes cannot be attributed to frictional instabilities across a fault plane, because of high frictional resistance to sliding at depth. A volumetric change associated with a phase transition, expected to occur at depth[1–3], is often invoked as the physical mechanism; if so, the resulting source mechanism should contain a major isotropic component. Although many researchers have attempted to observe such an isotropic component[4–10], no one has yet convincingly proved or disproved its presence. There exists a portion of the seismogram which is well suited to resolve the isotropic component of deep earthquakes but which has not been analysed by previous workers. Here I use this component in a systematic analysis of 19 large deep earthquakes, and show that no significant isotropic component (<10% of the seismic moment) exists. A sudden implosive phase change can thus be ruled out as the primary physical mechanism for deep earthquakes.

A point-source earthquake mechanism is most generally expressed by a symmetric second-order tensor called the seismic moment tensor[11,12] M_{ij} $(i, j = r, \theta, \phi)$. The moment-tensor formalism includes both the isotropic source model and a double couple (two perpendicular force dipoles, with equal magnitudes

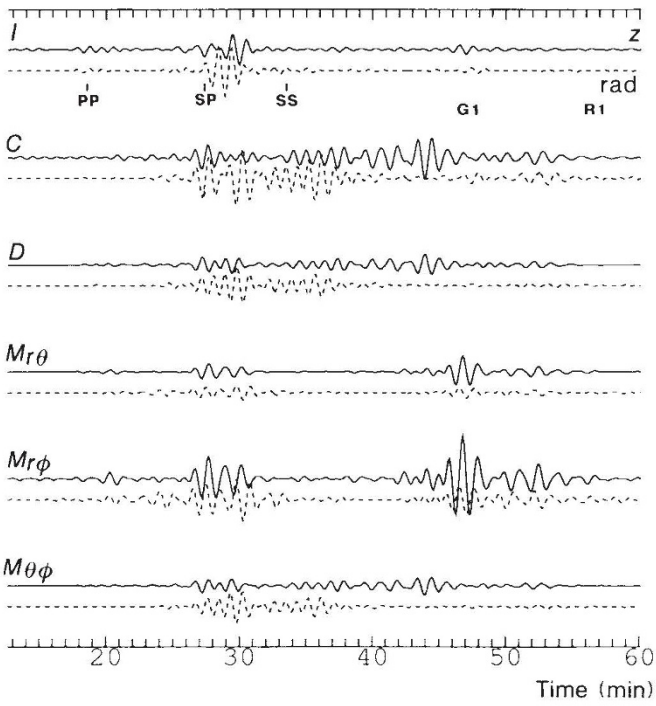

FIG. 1 Synthetic seismograms of long-period body waves for a deep earthquake. The earthquake is located at the hypocentre of the event south of Honshu and the station is BCAO (azimuth = 290°, Δ = 111°). The waveforms are calculated by a summation of normal modes and filtered between 10 and 22 mHz. For each pair of seismograms, the upper trace (solid line) is for the vertical component and the lower trace (dotted line) is for the radial component. Six pairs of seismograms are shown, one for each of six elements of the moment tensor. The diagonal components of a moment tensor are re-defined as $I=(M_{rr}+M_{\theta\theta}+M_{\phi\phi})/3$, $C=(M_{\theta\theta}+M_{\phi\phi}-2M_{rr})/3$, $D=(M_{\theta\theta}-M_{\phi\phi})/2$. Note that the body-wave waveforms for the isotropic component and C-component are quite different, but this is not the case for long-period surface waves. Expected arrival times of some important phases are also indicated.

but opposite signs), which corresponds to a slip on a planar fault, as special cases. A double-couple model has four degrees of freedom to specify a fault plane, a slip direction and a slip size, whereas a moment tensor generally has six degrees of freedom. These two excess degrees of freedom are called non-double-couple components of the moment tensor. It is common to separate a moment tensor into two parts, the isotropic component $I=(M_{rr}+M_{\theta\theta}+M_{\phi\phi})/3$ and the deviatoric part $M_{ij}-I\delta_{ij}$. Any deviatoric non-double-couple moment tensor can be expressed as a summation of two double couples, although the decomposition is not unique.

It is difficult to observe the isotropic component because the long-period surface-wave waveforms or narrow-band low-frequency normal-mode data excited by an isotropic source are very similar to those excited by another independent (deviatoric) component of a moment tensor, the vertical compensated linear vector dipole[4] (CLVD) component $C=(M_{\theta\theta}+M_{\phi\phi}-2M_{rr})/3$ (ref. 13). As most previous studies used only the above data, reported isotropic components, large or small, are subject to large uncertainty because of the presence of vertical CLVD components. Studies[4,14] using amplitudes of a few body-wave phases are also not promising, because many deep earthquakes are known to have complex source time-functions[15] and variable source mechanisms[16,17], and because the data coverage on the focal sphere is very limited. It is thus essential to analyse waveforms of many different body-wave phases to measure the isotropic component accurately.

The portion of the seismogram from the first P-wave arrival to just before the arrival of the first surface-wave train contains many different body-wave phases, including P, PcP, PP, PS and

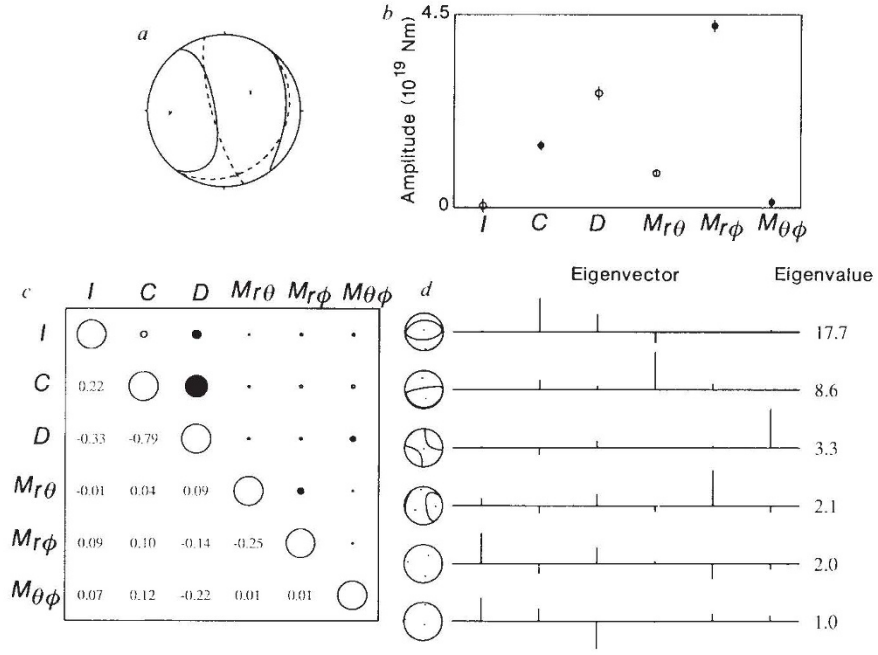

FIG. 2 Example of CMT inversion for the south of Honshu earthquake (1 January 1984, depth = 383 km). *a*, Equal-area projection (lower hemisphere) of the CMT solution. The solid lines show the nodal lines of the full moment tensor, with the shaded area indicating the positive first motion region. The dotted lines indicate the nodal lines of the double-couple model that shares the same principal axes as the non-double-couple (full) moment tensor. Note the large non-double-couple component. *b*, Relative amplitude of each component of the moment tensor. The error bars indicate one standard deviation. Open and closed circles indicate positive and negative values, respectively. Note that the isotropic component is almost zero. *c*, Corresponding correlation matrix. The diameter of circle is proportional to the magnitude of the correlation coefficient. Here the correlation coefficient between I and C is 0.22, whereas that with surface-wave data is 0.80, showing the superior resolution of I-component using long-period body-wave waveforms. *d*, Eigensolutions of the normal equation matrix. The lengths of the stick marks on each row give the contribution of moment-tensor elements for each eigenvector. The corresponding relative eigenvalues are given on the right and corresponding focal mechanisms on the left. A focal mechanism (that is, an eigenvector) that has a larger eigenvalue is better resolved with the given data set. The dots on the focal spheres indicate locations of the principal axes. Note that the eigenvectors that have significant isotropic components have the smallest eigenvalues.

others. Synthetic seismograms of such long-period (10–22 mHz) body waves for a deep earthquake indicate that the isotropic and the vertical CLVD components excite these waves quite differently (Fig. 1). It should therefore be possible to distinguish these two components by analysing long-period body waves; numerical experiments using these synthetic seismograms in fact prove that the isotropic component of a deep earthquake can be independently resolved by analysing long-period body-wave waveforms with sufficient station coverage (with stations every 30° both in longitudal and azimuthal directions, the correlation between two components can be <0.05 for deep earthquakes). Similar experiments with long-period (~150 to ~300 s) surface waves show a strong correlation between the isotropic component and the vertical CLVD component. The vertical CLVD component is often quite large for deep earthquakes. If the lateral heterogeneity of the Earth is not included in a model, such strong correlation with a presence of a vertical CLVD component can bias the estimate of the isotropic component[9,13].

The centroid-moment-tensor (CMT) inversion method of Dziewonski *et al.*[18], which simultaneously solves for a moment tensor and a spatio-temperoral centroid, is well suited for inverting these long-period body-wave phases to obtain the isotropic component of the moment tensor. Figure 2 shows the result of the CMT inversion of the above data for a deep (~380 km) earthquake which occurred south of Honshu, Japan on 1 January 1984. This event is well suited to test the method, because it has good station coverage and because it has a deviatoric non-double-couple moment tensor which is well documented[17,19] and large, indicating a somewhat unusual source mechanism. The correlation matrix indicates that the isotropic component is well resolved; the isotropic component obtained is essentially zero. Figure 2*d* indicates that the eigenvectors that have singificant isotropic components have the smallest eigenvalues. This suggests that it is still relatively difficult to observe the isotropic component even using long-period body-wave data. This is because the isotropic component is less efficient in exciting seismic waves in general, but the solution at least will not be biased by the presence of the vertical CLVD component.

To ascertain whether or not this result is general, we performed systematic body-wave CMT inversions for two sets of deep earthquakes. The first set consists of 9 events (including the earthquake on 1 January 1984) whose reported moment-tensor solutions[20] exhibit large deviatoric non-double-couple components. The second set consists of 10 events whose seismic moments are greater than 10^{19} N m. Figure 3 shows the moment-tensor solutions of the events in the first set. For all events that have large deviatoric non-double-couple components, the isotropic components are zero or negligible. Thus the large non-double-couple moment tensor observed for those events is entirely of deviatoric origin. For the event of 1 January 1984 it has been shown[17] that the large non-double-couple component observed at low frequencies can be explained by the presence of multiple subevents with different double-couple focal mechanisms separated in time by a few seconds, and does not require any isotropic component.

Figure 4 summarizes the size distribution of the isotropic component for all 19 deep earthquakes studied. The isotropic component is always ≤10% of the deviatoric seismic moment. Error bars covering two standard deviations always cut through the zero isotropic value. There seems to be no systematic difference between events with large non-double-couple components and those without. The sign of the isotropic component shows no systematic pattern, whereas an implosive phase change should always result in a negative isotropic component. These

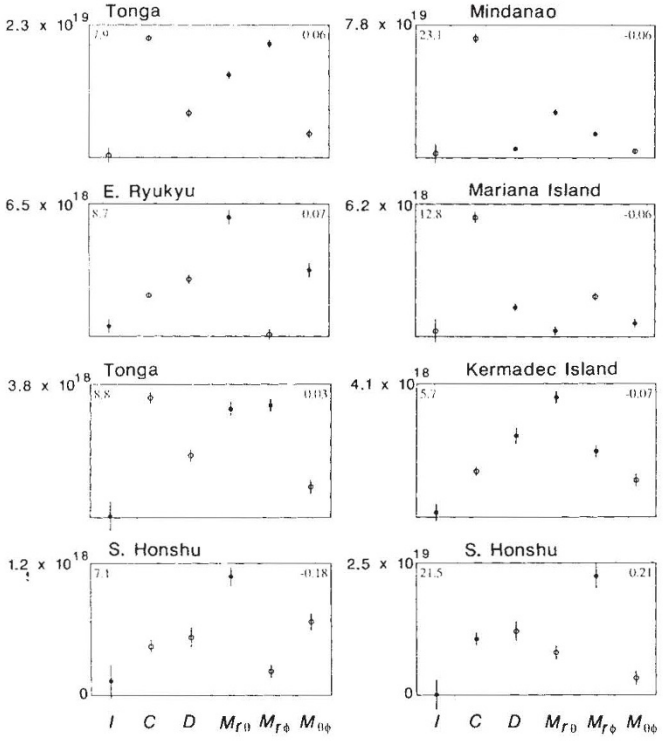

FIG. 3 Moment-tensor solutions for eight deep earthquakes which have a large deviatoric non-double-couple component (symbols as for Fig. 2*b*). The dates and depths of these earthquakes are: Tonga, 16 June 1986, 565 km; Mindanao, 5 March 1984, 630 km; east of Ryukyu, 4 July 1982, 554 km; Mariana Island, 4 January 1982, 590 km; Tonga 7 October 1981, 627 km; Kermadec Island, 28 September 1981, 335 km; south of Honshu, 31 March 1980, 359 km; south of Honshu, 7 March 1978, 434 km. The correlation coefficient between the *I* and *C* components, and the ratio of the maximum to minimum eigenvalues are shown at the right-upper and left-upper corner of each box, respectively. The ratio gives the condition number of the normal equation matrix; the smaller the ratio, the more stable the solution. Note that the vertical CLVD component (*C*) is often quite large for these events, and this can bias estimates of the isotropic component using long-period surface wave or free oscillation data. For all events, the isotropic components are essentially zero or negligible.

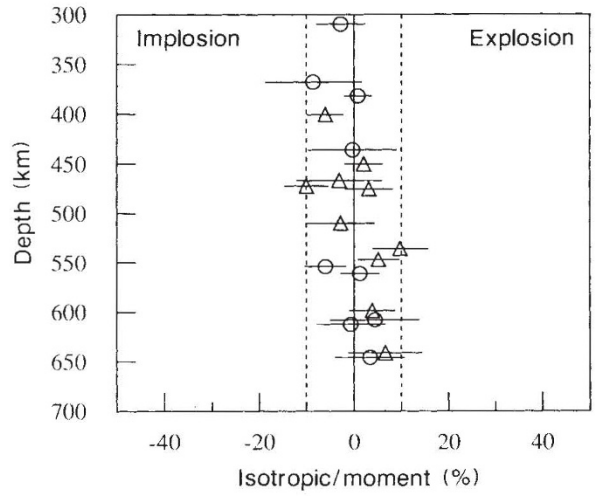

FIG. 4 Depth distribution of the isotropic components of all 19 deep earthquakes. The horizontal axis shows the size of the isotropic component as a percentage of the deviatoric seismic moment. The positive and negative values correspond to explosive and implosive isotropic sources, respectively. A deviatoric seismic moment is the average of the absolute values of the largest and smallest eigenvalues of a deviatoric moment tensor, $D_{ij} = M_{ij} - I \cdot \delta_{ij}$. The circles are for the nine events with large deviatoric non-double-couple components, and the triangles are for the ten events with seismic moments $>10^{19}$Nm. The horizontal error bars indicate one standard deviation. The vertical broken lines indicate ±10% isotropic values and all points are within this range. There seems to be no systematic pattern and no difference between the two sets of deep earthquakes.

observations also hold for smaller deep events[21]. I therefore conclude that the isotropic component of deep earthquakes is <10% of the seismic moment in the period range 45–100 s, that its presence is statistically insignificant, and that a sudden implosive phase change can be ruled out as the primary physical mechanism for deep earthquakes. This conclusion is consistent with recent laboratory experiments on metastable phase transformations[22,23], which suggest 'transformation faulting' as the physical mechanism of deep earthquakes without requiring a significant isotropic component[1]. □

Received 2 January; accepted 8 March 1991.

1. Bridgman P. W. *Am. J. Sci.* A**243,** 90–97 (1945).
2. Benioff, H. *Bull. seism. Soc. Am.* **53,** 893–903 (1963).
3. Evison, F. F. *Bull. seism. Soc. Am.* **57,** 9–25 (1967).
4. Randall, M. J. & Knopoff, L. *J. geophys. Res.* **75,** 4965–4976 (1970).
5. Dziewonski, A. M. & Giblert, F. *Nature* **247,** 185–188 (1974).
6. Gilbert, F. & Dziewonski, A. M. *Phil. Trans. R. Soc. Lond.* A**278,** 187–269 (1975).
7. Silver, P. G. & Jordan, T. H. *Geophys. J. R. astr. Soc.* **70,** 755–787 (1982).
8. Riedesel, M. A. & Jordan, T. H. *Bull. seismol. Soc. Am.* **79,** 85–100 (1989).
9. Okal, E. A. & Geller, R. J. *Phys. Earth planet. Inter.* **18,** 176–196 (1979).
10. Vasco, D. W. & Johnson, L. R. *Geophys. J.* **97,** 1–18 (1989).
11. Gilbert, F. *Geophys. J. R. astr. Soc.* **22,** 223–226 (1970).
12. Backus, G. & Mulcahy, M. *Geophys. J. R. astr. Soc.* **46,** 341–361 (1976).
13. Mendiguren, J. A. & Aki, K. *Geophys. J. R. astr. Soc.* **55,** 539–556 (1978).
14. Stimpson, I. D. & Pearce, R. G. *Phys. Earth planet. Inter.* **47,** 107–124 (1987).
15. Fukao, Y., & Kikuchi, M. *Tectonophysics* **144,** 249–269 (1987).
16. Strelitz, R. A. *Phys. Earth planet. Inter.* **21,** 83–96 (1980).
17. Kuge, K. & Kawakatsu, H. *Geophys. Res. Lett.* **17,** 227–230 (1990).
18. Dziewonski, A. M., Chou, T. A. & Woodhouse, J. H. *J. geophys. Res.* **86,** 2825–2852 (1981).
19. Ekström, G., Dziewonski, A. M. & Steim, J. M. *Geophys. Res. Lett.* **13,** 173–176 (1986).
20. Dziewonski, A. M., Franzen, J. E. & Woodhouse, J. H. *Phys. Earth planet. Inter.* **34,** 209–219 (1984).
21. Kuge, K. thesis, Univ. Tokyo (1991).
22. Kirby, S. H. *J. geophys. Res.* **92,** 13789–13800 (1987).
23. Green, H. W. & Burnley, P. C. *Nature* **341,** 733–737 (1989).

ACKNOWLEDGEMENTS. I thank B. Geller, G. Ekström and H. Houston for useful comments.

Lower-mantle viscosity constrained by seismicity around deglaciated regions

G. Spada*, D. A. Yuen†, R. Sabadini* & E. Boschi*

* Istituto di Geofisica, Dipartimento di Fisica, Università di Bologna, 40127 Bologna, Italy
† Department of Geology and Geophysics and Minnesota Supercomputer Institute, University of Minnesota, Minneapolis, Minnesota 55415, USA

KNOWLEDGE of the viscosity structure of the Earth's mantle is important for constraining models of mantle convection and isostatic rebound. Here we show that seismicity around the margins of deglaciated areas provides a constraint on the viscosity of the lower mantle, in addition to those previously proposed[1,2]. Calculations using a spherical, viscoelastic Earth model show that the present-day magnitude of the stress fields induced in the lithosphere beneath the (now-disappeared) Laurentide and Fennoscandian ice sheets is very sensitive to the value of the lower-mantle viscosity. Stresses of ~100 bar, sufficient to cause seismicity, can still remain in the lithosphere for lower-mantle viscosities greater than $\sim 10^{22}$ Pa s; for lower-mantle viscosities of $\sim 10^{21}$ Pa s, only a few tens of bars of stress persist in the lithosphere today. This influence of lower-mantle viscosity on the state of stress in the lithosphere also has implications for the migration of stress from earthquakes, and hence for earthquake recurrence times.

Estimates of mantle viscosity have been based on postglacial rebound[1] and geoid anomalies[2]. A stratified mantle with a lower-mantle viscosity of $\sim 10^{22}$ Pa s is favoured by geoid anomalies[2], whereas from global sea-level changes[3] a lower-mantle viscosity has been obtained that is slightly higher than the upper-mantle viscosity of 10^{21} Pa s. Lower estimates for the upper-mantle viscosity of $3–5 \times 10^{20}$ Pa s can be derived from sea-level curves in northwestern Europe[4]. The issue of mantle viscosity structure is by no means settled because of the intrinsic differences in the various data sets.

The seismic activity at passive continental margins in eastern Canada and Fennoscandia has been attributed to the melting of the Pleistocene ice sheets[5–7]. Estimates of stress fields[8] produced by removal of ice loads were based on the elastic plate flexure model and showed that considerable stresses ($\sim 10^2$ bar) could be produced on unloading. Stresses from glacial melting were also computed using a viscous rheology in a spherical model with both uniform and stratified viscosity profiles. For a uniform mantle viscosity[9], stresses of a few bars were found at the base of the lithosphere, whereas for individual long-wavelength harmonics[10] in the stratified models, much higher stresses ($\sim 10^2$ bar) still remained at the top of the mantle, and the lower-mantle viscosity was $\sim 10^{22}$ Pa s. For the timescales considered here ($\sim 10^4$ yr), mantle deformation processes are better described by viscoelastic rheology. A more realistic model is needed to investigate the problem of contemporary stress fields induced by deglaciation; this model should incorporate viscoelastic relaxation, as the consequences of stress fields in former deglaciated regions can affect the assessment of earthquake hazards[11].

We have employed a five-layer model[12], consisting of a purely elastic lithosphere, a three-layer viscoelastic mantle with a Maxwell rheology and an inviscid core, to provide a realistic description of the evolution of stress caused by deglaciation and to account for the presence of a high-viscosity transition zone[13] in the mantle. The shear modulus and density for each of the layers is taken from seismic estimates. The ratio of lower- to upper-mantle viscosity is denoted by B; in models with a high-viscosity transition layer, there is another parameter C, representing the ratio of the transition-zone viscosity to the upper-mantle viscosity.

Green's functions can be constructed analytically for the stress fields from the elastic and viscoelastic contributions to the displacement fields. For the axisymmetric spherical model, the viscoelastic stress-tensor components in the Laplace-transformed domain are:

$$\sigma_{rr}(r, \theta; s) = \Pi + 2\mu(s) \sum_{n}^{K} \dot{U}_n P_n \tag{1}$$

$$\sigma_{r\theta}(r, \theta; s) = \mu(s) \sum_{n}^{K} \left[\left(-\frac{V_n}{r} + \dot{V}_n \right) P_n - \frac{U_n}{r} \partial_\theta P_n \right] \tag{2}$$

$$\sigma_{\theta\theta}(r, \theta; s) = \sigma_{rr} + 2\mu(s) \sum_{n}^{K} \left[\left(\frac{U_n}{r} - \dot{U}_n - \frac{n(n+1)V_n}{r} \right) P_n - \frac{\cot\theta}{r} V_n \partial_\theta P_n \right] \tag{3}$$

$$\sigma_{\phi\phi}(r, \theta; s) = 2\sigma_{rr} - \sigma_{\theta\theta} + 4\mu(s) \times \sum_{n}^{K} \left(\frac{U_n}{r} - \dot{U}_n - \frac{n(n+1)V_n}{2r} \right) P_n \tag{4}$$

where r and θ are respectively the radius and the co-latitude coordinate, ϕ is the longitude, s is the Laplace-transformed variable, n is the angular order of the Legendre function $P_n(\cos\theta)$, σ_{ij} are the elements of the stress tensor in an axisymmetric spherical model, Π denotes the isotropic components, and the scalar functions U and V represent respectively the radial and tangential displacements. The dot denotes differentiation with respect to r. The index K, here taken to be 100, represents the highest angular order used in summing the contributions from different wavelengths excited by the disintegrating ice sheet. These stress fields are time-dependent because the transformed shear modulus $\mu(s)$, U_n and V_n are all functions of the Laplace-transformed variable s. A linear Maxwell